Laboratory Modelling of Sill Emplacement: Part 2 – sill segmentation

Uchitha N. Arachchige[1], Alexander R. Cruden[1], Roberto Weinberg[1]

[1]School of Earth, Atmosphere and Environment, Monash University, 9 Rainforest Walk, Clayton, VIC 3800, Australia

Abstract

It is increasingly recognised that most sheet-like igneous intrusions such as sills and dykes have segmented, rather than planar margins. The geometry of these segments and their connectors can provide insights into magma propagation pathways and host-rock deformation mechanisms during their emplacement. Here we report the results of scaled laboratory experiments on the emplacement of shallow-crustal, saucer-shaped sills with a focus on their propagation and segmentation. Visco-elasto-plastic Laponite RD® (LRD) and Newtonian paraffin oil were used as analogues for layered upper crust rocks and magma, respectively. Our results indicate that: 1) experimental saucer-shaped intrusions are highly segmented with marginal lobes and fingers; 2) the evolution and geometry of marginal segments and their connectors are different within the horizontal inner sill and the inclined outer sill; and 3) the bimodal nature of segment aspect ratios is linked to propagation of the inner sill along a horizontal host-rock interface versus interaction of the inclined outer sill with a homogenous upper layer. Measurements of inlet magma pressure and structural analysis suggest that marginal finger and lobe segments propagate in a repetitive sequence that starts with segmentation, followed by merging of segments and new growth of fingers/lobes. Based on the 3D geometry of segments, we suggest that sill segmentation is linked to smaller scale visco-plastic instabilities that occur within the inner sill and large scale mixed mode (I+III) fracturing during the inclined sheet propagations.

Plain Language Summary

Magmatic intrusions, such as “Sills” and “Dykes” are commonly considered as complex, irregular bodies which are known as segments. These segments usually consists of fingers or lobe like shapes and they are important geometrical features to understand the magma ascend through the Earth’s crust. . In order to understand how these segments form and propagate within rock layers, we analyse a series of laboratory experiments on “Saucer-shaped” sill

intrusions. We find that experimental saucer-shaped sills are highly segmented at their propagating margins and consists of different sizes of fingers and lobes. However, the length and the width of these segments are markedly different within the flat and inclined part of the saucer-shaped sills. Using their shapes and the help of the measurement of fluid pressure, we suggest that these segments propagate in a sequence that start with breaking, followed by merging and the growth of new segments.

1. Introduction

Igneous sheet intrusions, such as sills and dykes, play a dominant role in magma transport over large distances within the Earth's crust (Anderson, 1937; Ernst et al., 1995). These intrusions are generally considered to be planar bodies that interconnect to build complex sub-horizontal and sub-vertical magma plumbing systems (Magee et al., 2016; Muirhead et al., 2016; Cruden and Weinberg, 2018). However, field observations and 3D seismic surveys find that most sheet intrusions are segmented at their propagating margins into laterally and/or vertically offset magma lobes or fingers (Fig. 1) (Pollard et al., 1975; Thomson and Hutton, 2004; Hansen and Cartwright, 2006; Magee et al., 2016). The geometries of these segments are important because they are an indicator of magma propagation directions and emplacement mechanisms (Magee et al., 2019). However, determining the links between igneous intrusion mechanisms and segmentation is challenging because: i) field and seismic observations only reflect the final stage of the emplacement process; and ii) laboratory and numerical experiments have yet to produce complex segmentation patterns that are similar to those observed in nature.

Most research on the segmentation of igneous dykes and sills has taken a Linear Elastic Fracture Mechanics (LEFM) approach, in which segments are idealised as Mode I elastic fractures with tapered (wedge-shaped) or sharp tips (Pollard, 1973; Delaney and Pollard, 1981; Rubin, 1993). However, field and seismic studies indicate that sheet intrusions have segmented margins with finger-like or lobate forms with rounded and/or blunt tip geometries (Pollard et al., 1975; Hutton, 2009; Schofield et al., 2010; Spacapan et al., 2017; Galland et al., 2019). Various anelastic mechanisms, such as host rock fluidization (Schofield et al., 2010, Köpping et al., 2021), viscous indentation (e.g. Spacapan et al., 2017), and brittle shear faulting and/or ductile flow (e.g. Pollard and Johnson, 1973; Eide et al., 2017) have been proposed for segmentation of sheet intrusions with rounded or blunt tips. Therefore, the mechanisms that explain the formation of marginal intrusion segments are still debated.

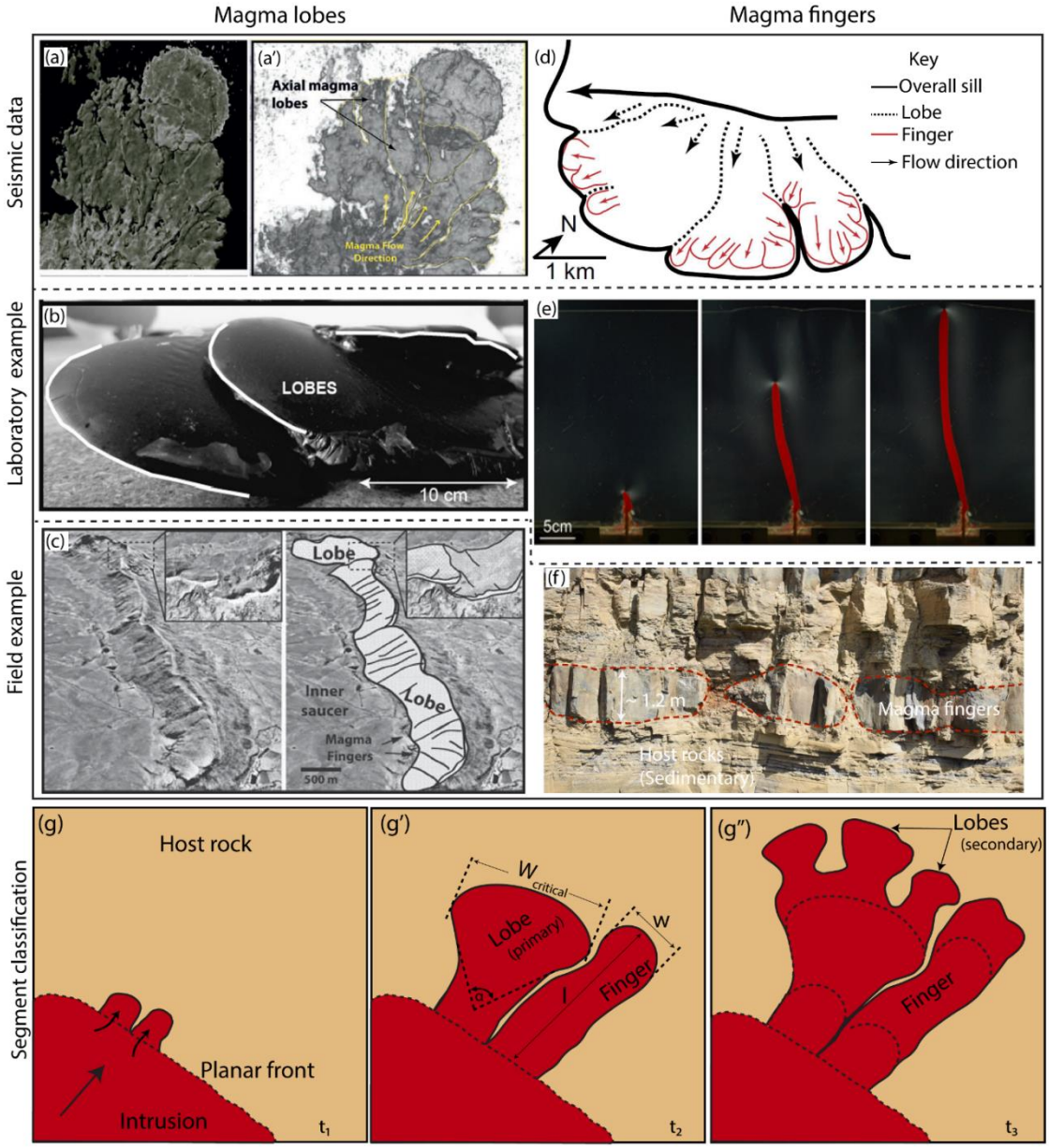

Figure 1: *A selection of sill segments observed in 3D seismic reflection data, field studies and laboratory experiments. (a) Magma lobes observed in 3D seismic reflection image of the Flat Ridge Sill, Faroe-Shetland Basin showing non-planar margins (from Schofield et al., 2012) and (a') an alternative view of (a) highlighting magma lobes and flow directions. (b) Lobes formed in a solidification experiment using hot vegetable oil injected into gelatine (from Chanceaux and Menand, 2014), and (c) lobes observed at the margin of the Golden Valley sill, Karoo Basin (from Schofield et al., 2010). (d) Magma lobes and fingers mapped in 3D seismic reflection data of a sill, Rockall Trough (from Magee et al., 2015, modified after Thomson and Hutton, 2004). (e) An analogue magma finger formed in a 2D Hele-Shaw cell experiment (from Bertelsen et al., 2018), and (f) magma fingers observed in the Shonking Sag laccolith, Montana (photo curtsey of Jonas Köpping). (g) Diagram illustrating the onset of non-planar margin at time step t_1, (g', g") definition of lobes, with an opening angle (α) and fingers, with sub-parallel sides ($\alpha \sim 0°$) at time step t_2 to t_3.*

Analogue experiments of igneous intrusions such as sills and dykes are important because their geometrical evolution can be monitored in three dimensions (3D). This can enable links to observations in nature to better understand their emplacement mechanisms and propagation pathways. Previous laboratory experiments on sill emplacement using granular materials (elasto-pastic; Galland et al., 2009; Mathieu et al., 2008), polymethyl methacrylate (PMMA) and glass (elastic; Bunger et al., 2008) and gelatine (visco-elastic; Kavanagh et al., 2006) as host rock analogues, mainly focused on the formation of planar and saucer-shaped intrusions. Lobate marginal segments were produced in experiments by Chanceaux and Menand (2016) and Currier and Marsh (2015) that included the effects of solidification during the emplacement and growth of sills and laccoliths. Such previous experimental work has yet to reproduce the complex segmentation of sill margins observed in nature (Thomson and Hutton, 2004; Magee et al., 2016), and with exception of work by Bertelsen et al. (2018) has usually neglected the complex visco-elasto-plastic rheological behaviour of rocks in Earth's upper crust. The mechanics of marginal segmentation in igneous intrusions is therefore poorly constrained and many fundamental questions about segmentation processes remain unanswered. For example, is it possible to produce lobes and finger segments in a laboratory experiments of sills? How does host rock rheology influence sill segmentation geometry and processes? How do marginal segments develop in space and time during the lateral propagation of sills?

Conversely, laboratory experiments on hydrofracturing within clay (ideally plastic material; Murdoch, 1993a, 1993b) and silica flour (elasto-plastic material; Chang, 2004; Wu, 2006) have generated complex non-planar fractures with lobe and finger segments. In a companion paper, Arachchige et al. (Chapter 3) report the results of analogue experiments using Laponite RD® (LRD), a visco-elasto-plastic host rock analogue, that focus on the formation and growth of saucer-shaped sills. Here, using a similar experimental approach, we

focus on the 3D geometry and formation mechanisms of complex marginal sill segmentation. Specifically, the aims of this contribution are to: (i) identify modes of sill segmentation that occur in visco-elasto-plastic host rock materials; (ii) determine how marginal segments develop in space and time during sill propagation; and (iii) investigate how marginal segments can be used to provide insights on the kinematics and dynamics of sill emplacement.

2. Background and methods

2.1. Segments, lobes and fingers

Many igneous sheet intrusions have highly segmented, non-planar margins (Pollard et al., 1975; Delaney and Pollard, 1981; Schofield et al., 2010; Magee et al., 2019). This segmentation often refers to the separation of originally planar intrusion margins into laterally and/or vertically offset, overlapping and/or underlapping individual structures known as *segments*, which are further subdivided into lobes and fingers (Fig. 1). These segments are also considered to form parallel to the propagation direction of the sheet intrusion (Schofield et al., 2012a). Moreover, at any given time during its propagation, the intrusion front may comprise two or more different segment types (i.e., lobes or fingers) with a range of sizes, which we will refer to as "complex segmentation".

In the context of igneous sills, the term *magma lobe* (Fig. 1) refers to a near-circular to elongated lobe-shaped geometry (Miles and Cartwright, 2010; Schofield et al., 2012). Here, we define a lobe to be a segment that widens in the intrusion propagation direction, with a positive opening angle, α between the two sides of the lobe (Fig. 1g′). Indeed, the formation of lobes in intrusions has been compared to pahoehoe lobes in lava flows, which form due to magma cooling and solidification at the flow front (Griffiths, 2000; Miles and Cartwright, 2010). During flow of lava, a partially chilled front is formed at the lava-water or lava-air contact, which inhibits the lateral spreading of lobes due to an increase in tensile strength. However, during continuous lava supply, internal pressure overcomes the local tensile strength

of the solidified front and lava bursts open through previously solidified lobes resulting in lateral growth and formation of new pahoehoe lobes. An analogous process has also been used to explain near-circular lobe-shape geometries in sills emplaced at shallow levels, such as the Solsikke Sill (Hansen and Cartwright, 2006), Vigra sill complex (Miles and Cartwright, 2010) and Golden Valley Sill (Schofield et al., 2010).

The term *magma finger* (Fig. 1) commonly describes elongated, narrow segments with an array of blunt and/or bulbous-ended tubes in dykes and sills (Pollard et al., 1975; Schofield et al., 2010; Spacapan et al., 2017; Galland et al., 2019). Here we define a finger as a parallel sided segment with an opening angle $\alpha \sim 0°$. Fingers mostly propagate along the same stratigraphic level and can be a few centimetres to hundreds of meters long (Magee et al., 2018). However, small vertical offsets of fingers may occur due to the exploitation of preferentially oriented, pre-existing weaknesses, which result in inconsistent stepping directions (Magee et al., 2019). Vertically and horizontally separated fingers can later coalescence, developing cusp-shaped grooves in between them (Pollard et al., 1975; Schofield et al., 2010, 2012a). The emplacement of magma fingers is commonly attributed to: i) viscous fingering instabilities (e.g., Saffman-Taylor instability) between a propagating magma front and a fluidised host rock (Pollard et al., 1975; Schofield et al., 2010); or ii) mixed mode (Mode I+III) fracturing within an elastic host material (Pollard and Johnson, 1973; Pollard et al., 1982).

2.2. Segment connectors

Segment *connectors* connect overlapping and/or underlapping segments. Known as steps, bridges, broken bridges and en-echelon structures (Fig. 2), they are often attributed to brittle magma emplacement mechanisms (Schofield et al., 2012a; Nicholson and Pollard, 1985; Hutton, 2009). Delaney and Pollard (1981) defined bridges as ‘curved slabs of rock that separate two neighbours in the echelon array’. Bridges of host rock strata (Fig. 2a) occur when two separate overlapping, vertically offset segments propagate simultaneously. As continuous

magma supply inflates the segments, bending of the intervening host rock strata occurs, resulting in a bridge structure (Schofield et al., 2012a). If further inflation and bending occurs, tensile fractures eventually develop perpendicular to the bridge axis, close to the zones of maximum flexure, forming a broken bridge between overlapping segments. Once bridges detached from both ends, they become xenoliths, or 'bridge xenoliths' within segments (Rickwood, 1990).

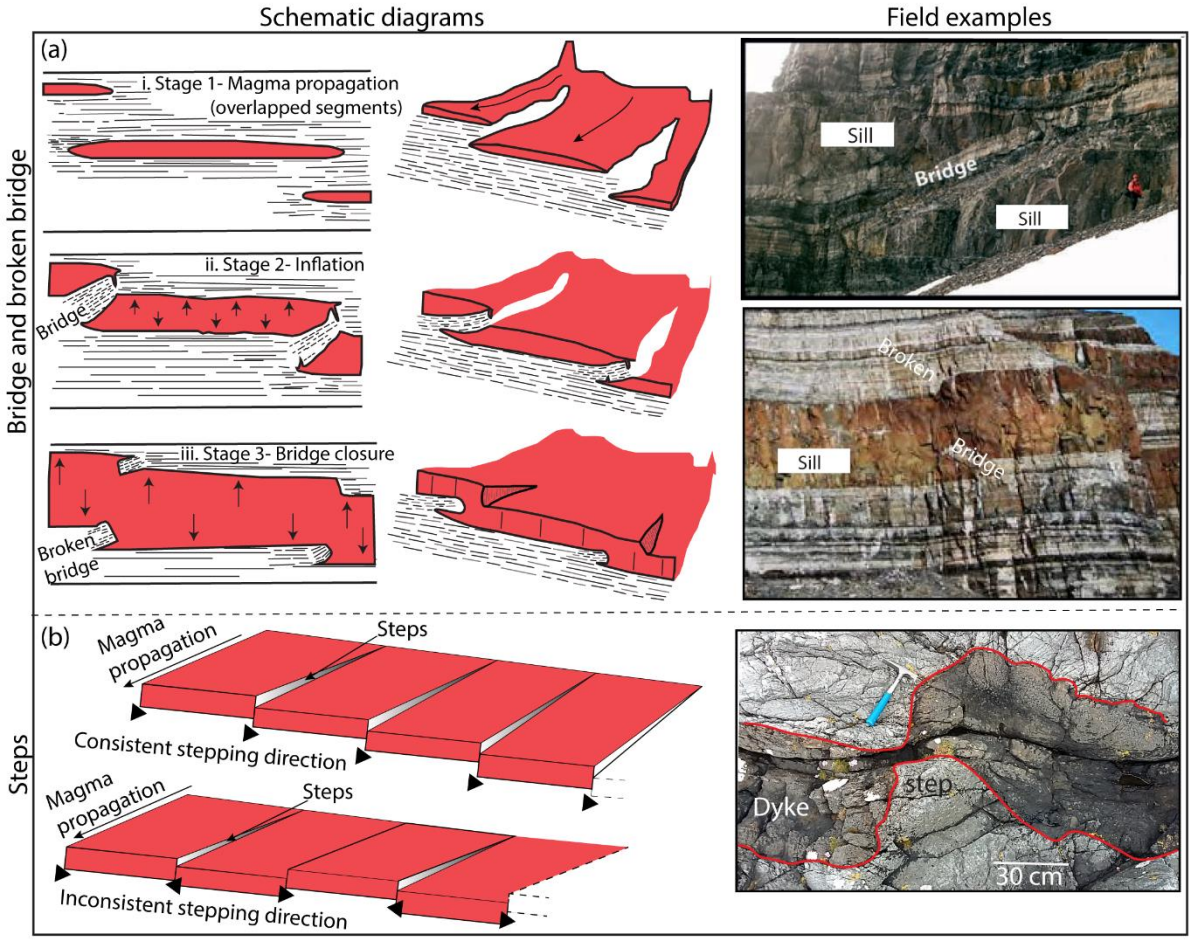

Figure 2: *A summary of segment connectors. (a) Left: schematic diagrams of bridge and broken bridges in cross-section and 3D in relation to: (i) overlapping segments; (ii) segment inflation; and (iii) bridge closure (after Eide et al., 2016). Right: field examples from the Theron Mountains, Antarctica (modified after Hutton, 2009). (b) Left: schematic diagrams of en-echelon steps in sills with consistent and inconsistent stepping directions. Right: steps developed in Mesozoic limestone and shale metasedimentary strata on Ardnamurchan, NW Scotland (modified after Magee et al. 2018).*

Steps form from initially vertically offset segments or en-echelon intrusion tips, which later coalesce into a single sheet as an intrusion propagates and inflates (Fig. 1b) (Schofield et al., 2012a; Eide et al., 2017). Steps between connected segments are oriented perpendicular to the direction of magma flow (Schofield et al., 2012b).

2.3. Experimental methods

This is the second of two companion papers that report the results of scaled laboratory experiments on the emplacement of sills in layered and non-layered elasto-visco-plastic analogue host rock materials. The complete series of laboratory experiments are described in Part 1 (Arachchige et al., in review), which focuses on the development of saucer-shaped sills. Here, in Part 2, we focus mainly on experiments in which saucer-shaped sills propagate with highly segmented margins with complex geometries.

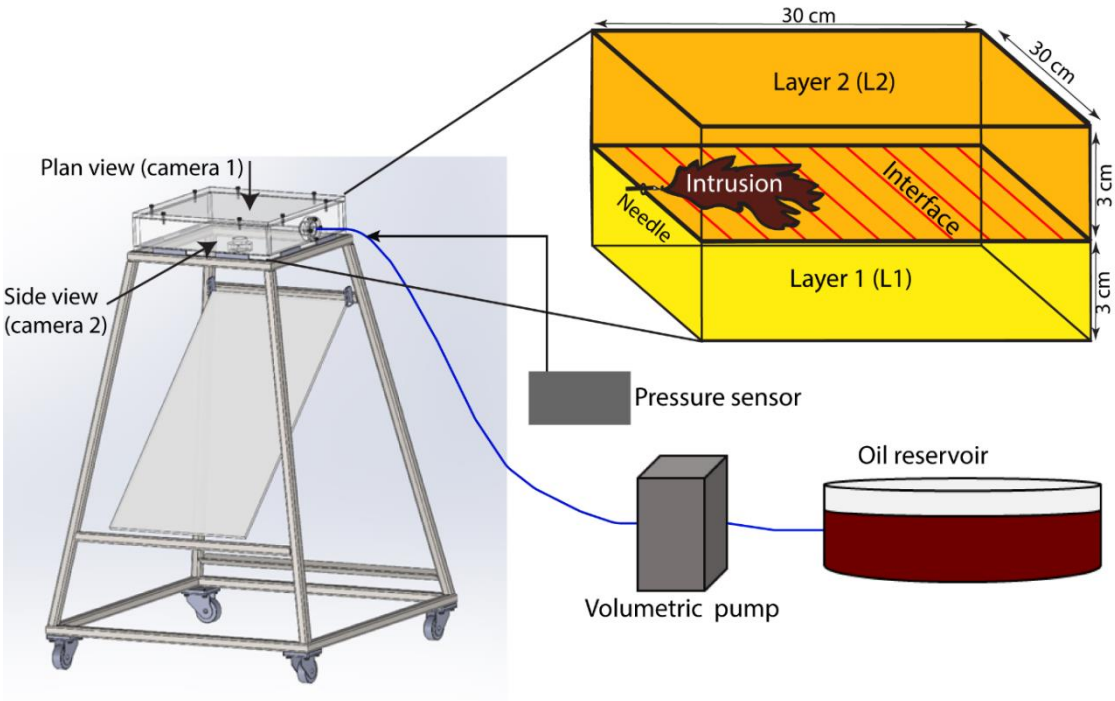

Figure 3: *Schematic diagram of the experimental setup (modified after Arachchige et al., Chapter 2). A volumetric pump injects paraffin oil into homogenous or layered Laponite RD® though a fixed hole using a needle. Two DSLR cameras capture the intrusion growth from top and side views respectively. The pressure sensor connects to the fluid flow just before the injection needle.*

The experimental setup comprises a plexiglass tank (30 cm x 30 cm x 6 cm) filled with elasto-visco-plastic Laponite RD® (LRD; Arachchige et al., 2021), the upper-crustal rock analogue (Layer 1 [L1] and Layer 2 [L2], Fig. 3). Paraffin oil (magma analogue) is injected horizontally into the interface between two 3 cm thick layers of LRD using a 2 mm diameter tapered needle via a nozzle at the side of the tank, which is fed at a controlled volumetric flow rate either by a peristaltic pump or a syringe pump. In all experiments, the Young's modulus of the upper (E_u) and the lower (E_L) layers are varied by changing the wt. % concentrations X_u and X_L of LRD in water. All other parameters such as the analogue magma volumetric flow rate (Q_i) and viscosity (μ), and the intrusion depth (3 cm) are constant. Propagation of the model intrusions is monitored by high-resolution DSLR cameras (Fig. 3) placed above and at the side of the experiment, providing plan and cross-sectional views, respectively. Two experiments (exp. 5, 6) were repeated using a syringe sump and a digital pressure sensor to measure pressure variations at the inlet of the intrusion (Fig. 3). The pressure sensor was calibrated to correct for any background signals from the syringe pump. Therefore, the pressure signals reported here only represent the fluid pressure at the inlet during the emplacement and growth of the model intrusions.

2.4. Model materials and scaling

We use Laponite RD® (LRD), a gel-forming grade of synthetic smectite clay manufactured by BYK Additives and Instruments (2014) and paraffin oil as the crustal host rock and magma analogues, respectively. When mixed with water, LRD forms a colourless, transparent and photo-elastic gel, which is similar to gelatine but chemically and biologically more stable (Ruzicka and Zaccarelli, 2011). LRD has lower surface energy values (24 - 44 mJ/m^2; Norris et al., 1993) compared to gelatine, a frequently used intrusion host rock analogue (1 J/m^2; Kavanagh et al., 2013). This ensures that surface tension dynamics are minimized in geological analogue experiments using LRD. The mechanical properties of LRD, such as

Young's modulus, can be easily varied by changing its concentration and curing time (Arachchige et al., 2021). Arachchige et al. (2021) recently showed that LRD is suitable for analogue modelling of visco-elasto-plastic rock deformation, including elastic and plastic end member behaviours. Shear strains, $\gamma < 10\%$ and strain rates of up to 0.01 s^{-1} for concentrations from 2 wt. % to 4 wt. % and a curing time of 72 hours must be maintained to model elastic dominant deformation. LRD starts to yield at a shear strain $\gamma = 10$ % for concentrations 2 wt. % to 4 wt. % with yield strength values varying from 25 to 200 Pa, respectively. Higher shear strains ($\gamma > 26.2$ %) and strain rates $\dot{\gamma} \geq 0.01$ s^{-1} must be maintained to model plastic deformation. We use the Young's modulus value of LRD as the main host rock variable and, following Arachchige et al. (2021), assume that LRD is incompressible with Poisson's ratio = 0.5. Paraffin oil (magma analogue) has a viscosity of 0.16 Pa s at 22.5 °C and, unlike water, it does not react with LRD. Paraffin oil was mixed with red dye to provide a better visual contrast with the host material without altering its viscosity.

The scaling of the experiments and the suitability of the model materials (Table 1) are described in detail by Arachchige et al. (2021) and Arachchige et al. (Chapter 3). The principle we follow is to define scaling factors for the models, which satisfy approximate geometric, kinematic and dynamic similarity to processes in nature (Hubbert, 1937; Ramberg, 1967; Galland et al., 2009).

We define the length scale factor (L*) as the ratio between the overburden depth of the sill in the model (subscript m) to one in the shallow crust (subscript p), which is initially taken to be 10^{-4} (1 cm in the laboratory represents 100 m in nature). The ratio between the density of LRD in the experiments and that of natural host rocks (ρ*) is ~ 0.36 and the gravitational acceleration is the same in our experiments and in nature (g* = 1). Thus, the stress scaling factor is:

$$\sigma^* = \rho^* g^* L^* = 3.6 \times 10^{-5} \quad (1)$$

Table 1. *Symbols, units and values of variables in nature and model*

Parameter	Dimension	Definition	Value		
			Nature (p)	Model (m)	Ratio*(m/p)
ρ_h	Kg m^{-3}	Density of host rock	2800	1000	0.357
ρ_i	Kg m^{-3}	Density of intrusions	2700	850	0.3
g	m s^{-2}	Gravity acceleration	9.81	9.81	1
V_i	m s^{-1}	Velocity of intrusion	0.2	10^{-5}	5 x 10^{-5}
L	m	Length	100	0.01	10^{-4}
t	s	Time	-	900-2700	2 x 10^{-2}
μ	Pa s	Viscosity of intrusion	2.2 x 10^5	0.16	7.14 x 10^{-7}
Q_i	m^3 s^{-1}	Volumetric flow rate of intrusion	(0.02 - 13.28)	8.3 x 10^{-9}	(6.25 x 10^{-10} - 3.75 x 10^{-7})

Stress scaling factor	**$\sigma^* = \rho^* g^* L^* \rightarrow \sigma^* = 3.57 \times 10^{-5}$** Model is 10^5 times weaker than in nature
Time scaling factor	**$t^* = L^*/V^* \rightarrow t^* = 2 \times 10^{-2}$** 1 min in model ~ 0.83 hr in nature
Viscosity scaling factor	**$\mu^* = t^* \sigma^* \rightarrow \mu^* = 7.14 \times 10^{-7}$** Model intrusion represents a magma viscosity of 10^4 Pa s
Volumetric flow rate scaling factor	**$Q^* = \Delta\rho^* L^{*3} E^{*-1} V^* \rightarrow Q^* = (6.25 \times 10^{-10} - 3.75 \times 10^{-7})$** Model represents natural flux range (0.02 – 13.28) $m^3 s^{-1}$

We compare the average model intrusion velocity of ~ 1 x 10^{-3} ms^{-1} to an estimated natural magmatic intrusion velocity of 0.2 ms^{-1} (within a range between 0.1 ms^{-1} and 0.5 ms^{-1} ;Spence and Turcotte, 1985; Kavanagh et al., 2013), which gives a velocity scaling factor, V* = 5 x 10^{-3}. We can now define the time scaling factor as

$$t^* = L^*/V^* = 2 \times 10^{-2} \quad (2)$$

Therefore, 1 min in our experiments represents 0.83 hr in nature. Using σ* and t*, the viscosity scaling factor becomes

$$\mu^* = \sigma^* t^* = 7.2 \times 10^{-7} \quad (3)$$

so paraffin oil (magma analogue) with a viscosity of 0.16 Pas is equivalent to a magma in nature with a viscosity of 10^4 Pas, consistent with basaltic andesite with low crystal content (Mathieu et al., 2008).

The measured Young's modulus, E, of LRD concentrations after 7 days curing time used in the experiments is 10^3 - 10^4 Pa (Arachchige et al., 2021)A. Since E of upper crustal sedimentary rocks is typically in the range of 10^9 - 10^{10} Pa (Kavanagh et al., 2013), the Young's modulus scaling factor, E* in our experiments is 10^{-7} – 10^{-5}. Therefore, based on σ* and E* our model host rock is 10^5 times weaker than in nature.

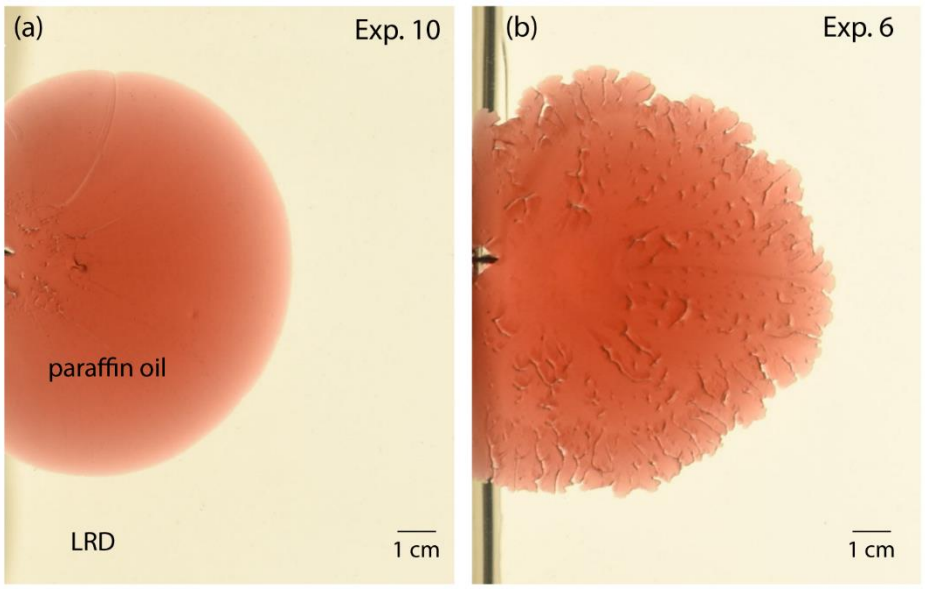

Figure 4: *(a) Comparison of the margins of experimental sills in plan-view. (a) Exp. 10 shows simple planar front whereas (b) Exp. 6 is highly segmented with finger and lobate geometries.*

3. Results

Here we focus on five experiments (Table 2) in which saucer-shaped sills formed with highly segmented intrusion fronts and complex geometries. In all experiments, an initial, flat, penny-shaped inner sill propagates along the interface between the two layers of LRD. This sill then bends upwards and intrudes the upper layer as an inclined outer sheet to form a saucer-shaped intrusion before the analogue magma erupts onto the model surface. Except for Exp. 10 (Fig. 4a) where the sill margin is planar, the propagating fronts of all intrusions are highly segmented with lobes and fingers. We further categorise these segments as being first (primary) and second (secondary) order (Figure 1g), discussed below.

The propagating margins of sills in our experiments have more complex geometries than the planar cracks that are typically formed in models using granular elasto-plastic (Mathieu et al., 2008; Galland et al., 2009) or visco-elastic (e.g., gelatine; Kavanagh et al., 2006) host materials. The inner flat sill and the outer inclined sheet of the saucer-shaped intrusions in our experiments have dominantly non-planar margins characterised by lobes and finger-like segments (e.g., Exp. 6; Figs. 4 and 5).

Table 2. *Summary of experiments and parameters*

No	X_{LL} (wt. %)	ρ_{LL} (kg m^{-3})	E_{LL} (Pa)	X_{UL} (wt. %)	ρ_{UL} (kg m^{-3})	E_{UL} (Pa)	E_{UL}/E_{LL}	comments
5	3	1050	5013	4	1075	10266	2.05	Flat sill to inclined saucer
6	3	1050	5013	3	1050	5013	1	Flat sill to inclined saucer
9	3.5	1060	8317	4	1075	10266	1.23	Flat sill to inclined saucer
30	3.5	1075	8317	3.5	1060	8317	1	Flat sill to inclined saucer
10	4	1075	10266	4	1075	10266	1	Flat sill to inclined saucer

X = concentration of Laponite RD® (LRD) in deionised water (wt. %); ρ is density of LRD (kg m^{-3}); E = Young's modulus of LRD (Pa). Rigidity ratio (E_r) = E_{UL}/E_{LL}

Subscripts LL = lower layer and UL = Upper Layer.

Taking Exp. 6 as a representative example, the inner sill is initially penny shaped with a planar margin that is confined to the interface between the two LRD layers (Fig. 5a). At t = 245 s the sill margin starts to break down into segments (Fig. 5a′, 5b). At this early stage, the segments are relatively large 1st order lobes fed by primary fluid flow vectors (Fig. 5d). Upon reaching a critical width, these segments bifurcate into smaller, second order lobes and fingers fed by secondary fluid flow vectors (Fig. 5e and supplementary Movie 1). As the inner sill propagates along the L1/L2 interface the segments evolve in the sequence: (1) fingers/lobes form at the intrusion front, (2) fingers/lobes merge laterally (i.e. segment coalescence), becoming wider, and (3) these break down again into narrower, secondary fingers/lobes. The segments that develop during propagation of the inner sill are also two dimensional (2D) structures confined to the L1/L2 interface.

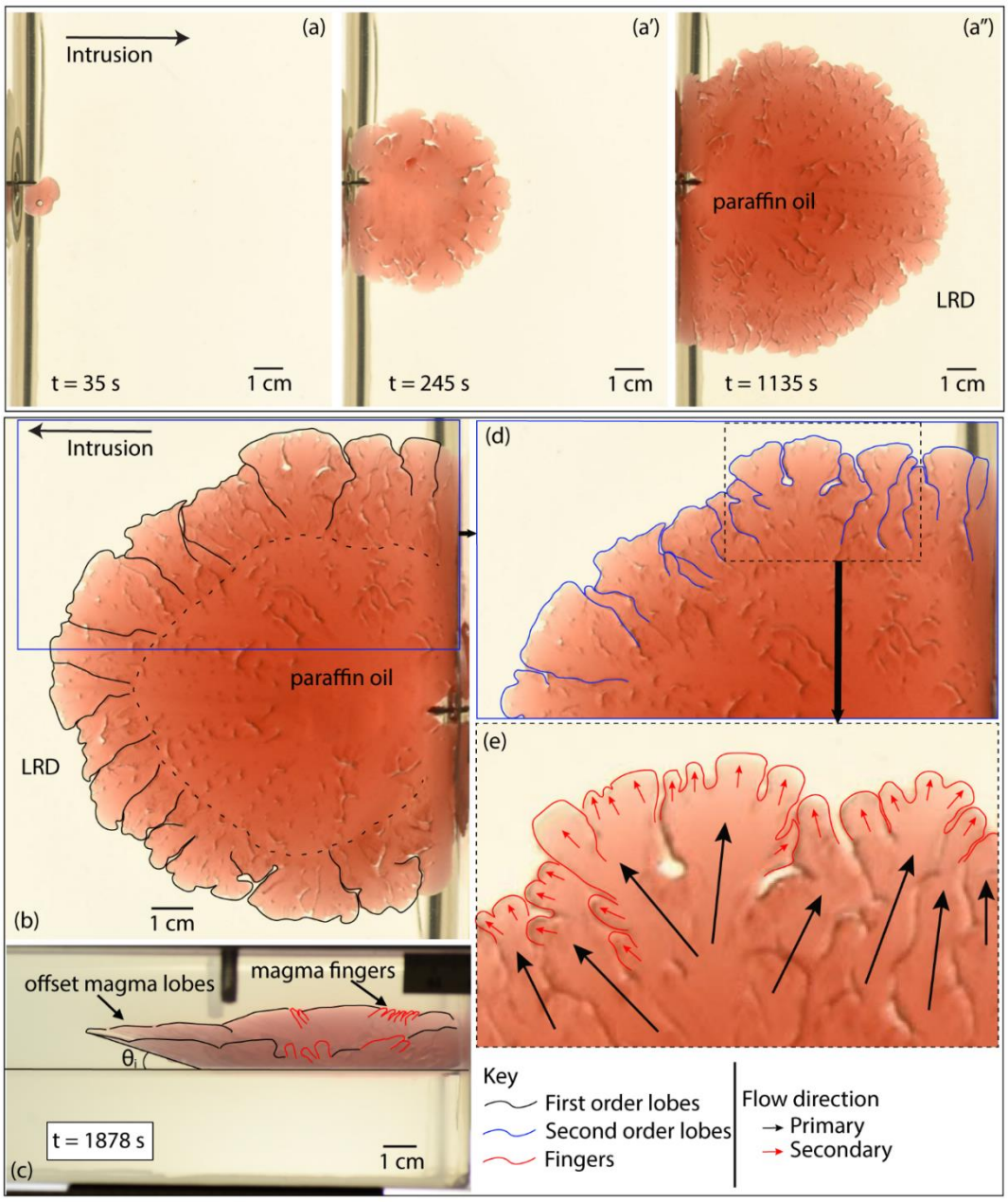

Figure 5: *Non-planar sill margin and segmentation formed in Exp. 6: (a-a") Plan view images. Paraffin oil (red) is injected from the left through a needle into transparent Laponite RD® (LRD). Arrow indicates sill propagation direction. (b) Plan view at a later time step than (a") rotated and magnified for a comparison with side view (c). The sill expands radially and breaks into lobes and fingers. Lobe segments show distinct 1st order (i.e. primary lobes, outlined in black) and 2nd order (i.e. secondary lobes, outlined in blue; or finger-like segments, outlined in red). The corresponding primary and secondary flow directions within the sill are shown ad black and red arrows, respectively. The dashed black line in (b) represents the transition from the horizontal inner sill to the inclined outer sheet, defining the saucer-shaped geometry observed in side view in (c). Vertically offset lobes and fingers only formed within the inclined sheet.* θ_i *is the dip of the inclined sheet. (d) and (e) are magnified sections of (b) and (d), respectively.*

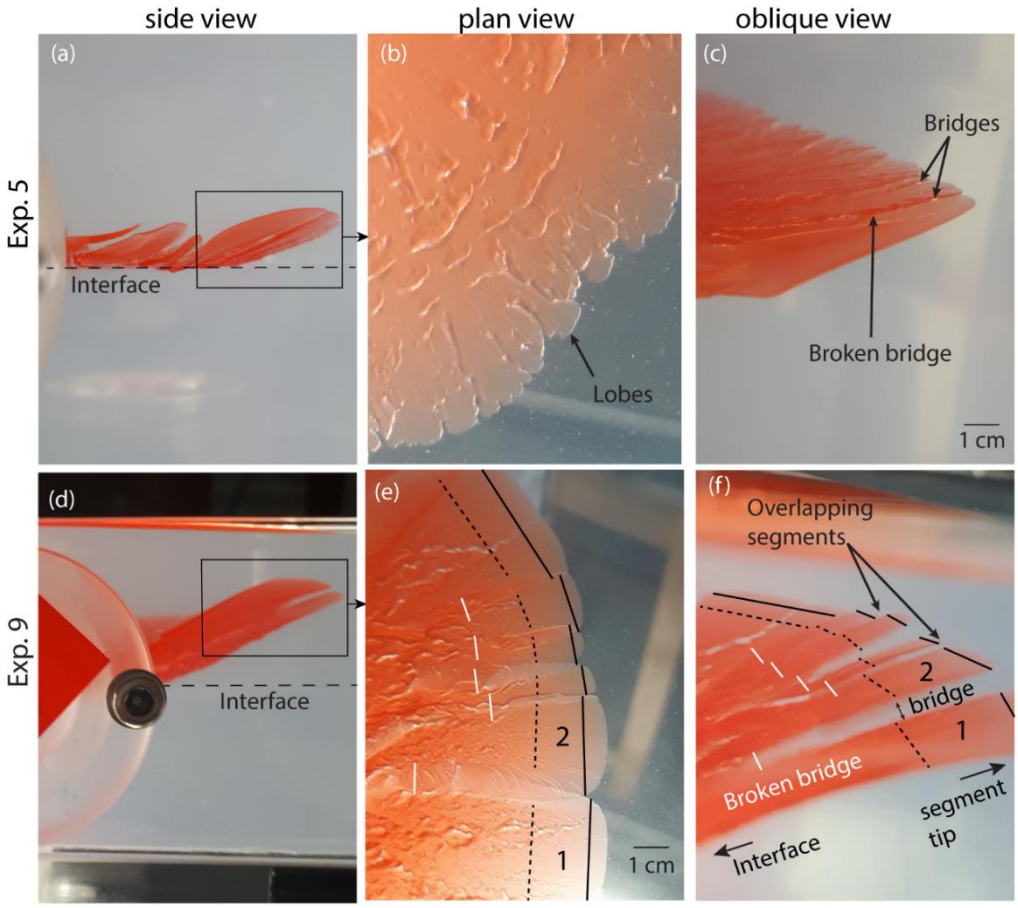

Figure 6: *Formation and evolution of segment connectors in Exp. 5 and 9 within inclined outer sheets in side (left), plan (middle) and oblique (right) view. In Exp. 5 (a-c) and Exp. 9 (d-f) the propagation front is non-planar and characterised by vertically displaced overlapping lobes. Bridges form closer to the centre of adjacent segments (e.g., dotted lines in segment 1 and 2; e, f) and broken bridges form closer to the layer interface (white lines) due to inflation of the segments (c, f). See text for details.*

Eventually the inner sill abandons the L1/L2 interface and intrudes upward into the homogenous L1 upper layer. During this new stage of sill growth, marginal segments form overlapping, en-echelon 3D structures. Figure 6 shows segments within the inclined outer sheets of Exp. 5 and 9 and the formation of segment connectors. These segments propagate along vertically and horizontally offset planes, and over time they thicken and connect resulting in segment connectors such as bridges and broken bridges (Fig. 6). At any given time, close to the tip of two adjacent segments (e.g., black lines in segment 1 and 2; Fig. 6e, f), the vertical offset is higher (i.e., overlapping segments). Towards the middle of the same segments (dashed lines in; Fig. 6e, f), a narrow space (i.e., bridge; Figs. 6c, f) of the host rock analogue is created

due to the inflation of the segment. Approaching the main body of the sill (white lines in; Fig. 6e, f), the narrow bridge of host rock closes and overlapping segments coalesce vertically (i.e. broken bridge; Figs. 6f and 1c).

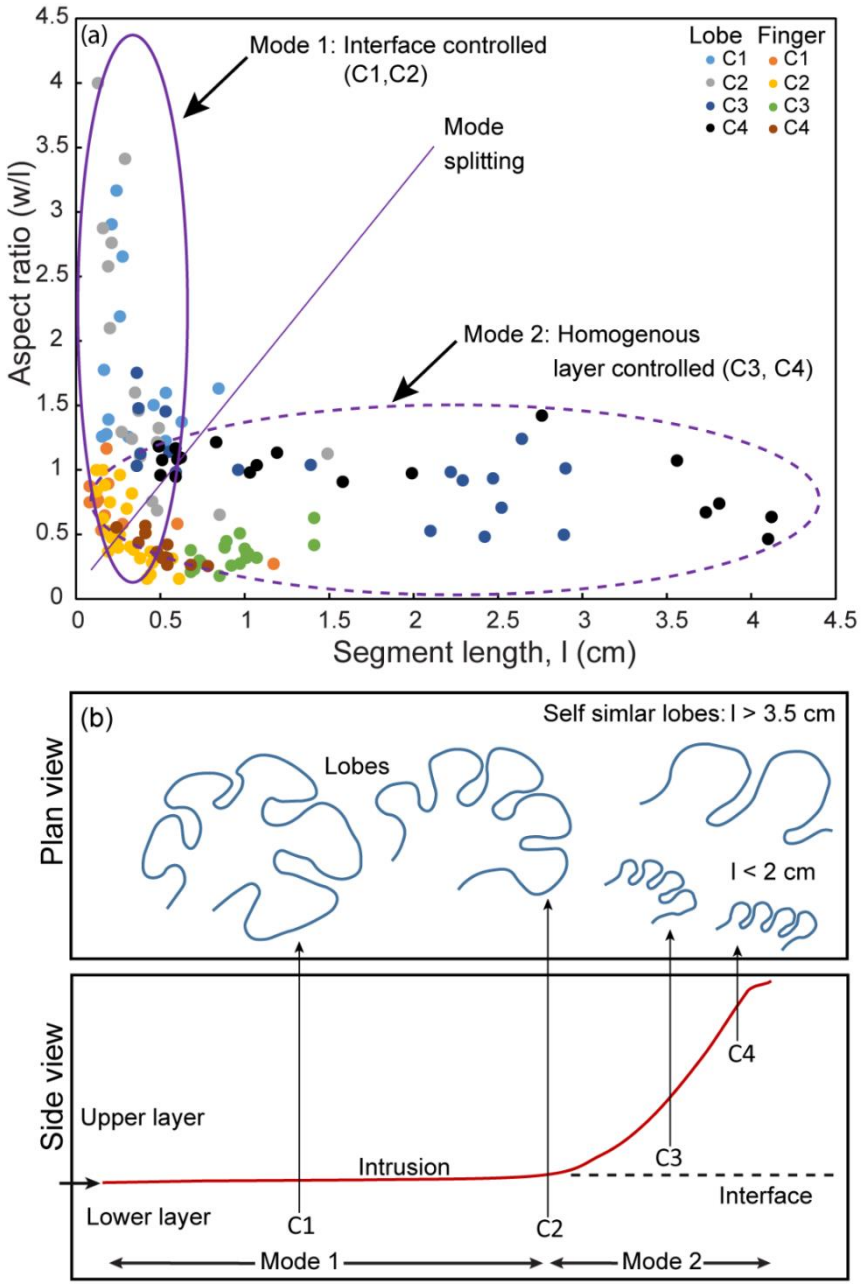

Figure 7: *(a) Plot of segment aspect ratio (width (w)/length (l)) versus segment length (l) measured at four locations (C1-C4) along the length of the intrusion indicated in (b) for all experiments. The two ellipses in (a) represent Mode 1 (interface-controlled) and Mode 2 (unconfined, formed within homogenous layer) type segments, respectively. Mode 1 segments are characterized by varying aspect ratios with relatively short lengths, whereas Mode 2 segments have similar aspect ratios over a range of lengths. (b) Representative plan view outlines of lobe segments at positions C1 to C4 indicated in the lower side view diagram.*

342 **3.1. Aspect ratio analysis**

343 Figure 7 plots the width/length (w/l) aspect ratios of lobe and finger-like segments in
344 plan view from all experiments measured at four locations along the radius of the intrusion (C1
345 – C4; Fig. 7b). The aspect ratios of finger-like segments are < 1 and cluster at w/l ~ 0.5. This
346 ratio decreases as the intrusion propagates from the inner sill to the inclined sheet (C1 to C4).
347 In contrast, the aspect ratios of lobe segments define two distinct groups when plotted against
348 length (Fig. 7a). The first group (Mode 1) forms while the sill propagates along the L1/L2
349 interface between the two LRD layers (C1 and C2). These "interface-controlled" lobe segments
350 have constant, relatively short lengths (<0.5 cm) while the aspect ratio increases as the sill
351 expands from C1 to C2. The second group (Mode 2) forms within the homogenous upper layer
352 (C3 and C4). These "unconstrained" lobe segments have small aspect ratios (0.5 - 1.5) and they
353 are up to 4 cm long. We consider Mode 2 to be unconstrained because the segments develop
354 within the homogeneous upper layer where lobes exploit the 3D space ahead of the tip of the
355 expanding sill. This implies that when lobes expand in a homogeneous material they tend to
356 maintain an approximately constant aspect ratio of ~ 1 as they lengthen (Fig. 7b).

357 **3.2. Inlet pressure measurements**

358 The pressure measured at the inlet of the needle during sill intrusion in Exp. 5 is plotted
359 against time in Figure 8. Peak pressure coincides with intrusion initiation. The pressure then
360 gradually drops with time as the sill radius increases, showing minor fluctuations (Fig. 8a). The
361 initial pressure drop occurs without fluctuations, corresponding to the period when the sill
362 propagates as a planar crack (Fig. 8a). At the end of this period, the intrusion starts to form a
363 lobate margin. From this point onwards the pressure curve fluctuates within a broadly
364 decreasing trend. Short wavelength periods of rising pressure (e.g., circled in Fig. 8b) occur
365 during growth of first order lobes at the propagating front of the intrusion. Minor pressure
366 variations during such periods of slightly increasing pressure corresponding to the growth of

second order lobes and fingers (Fig. 8c). In contrast, the following periods of decreasing pressure correspond to times when earlier formed primary and secondary segments coalesce. There is no obvious change in the pressure curve when the horizontal inner sill (HIS) transitions to the inclined outer sheet (HIS-IS transition in Fig. 8a).

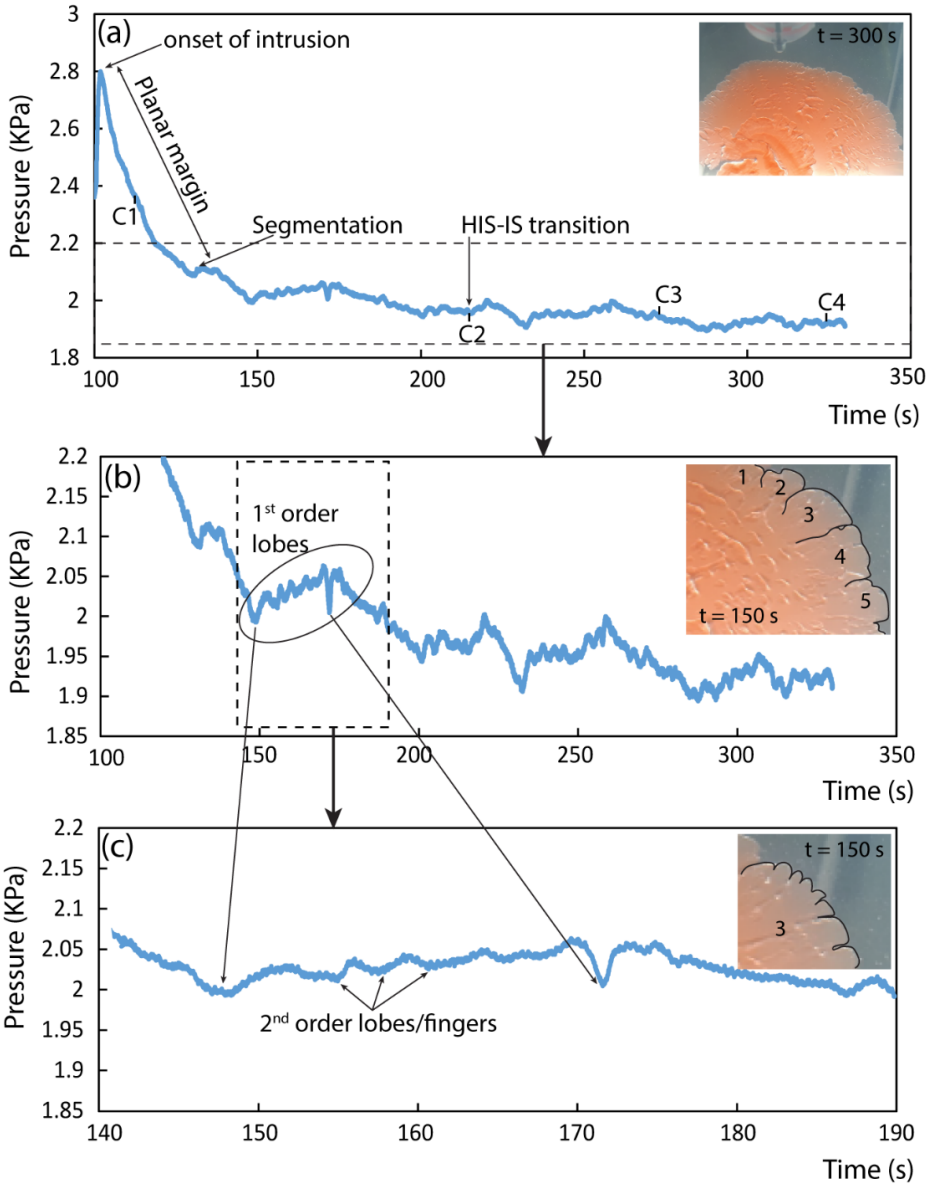

Figure 8: *(a) Injection pressure measured during sill emplacement in Exp. 5. Locations of aspect ratio measurements (C1-C4) and the horizontal inner sill to inclined sheet transition (HIS-IS) are indicated. Inset photograph shows the planar sill margin during initial growth stages. (b) Detail of part of (a) showing pressure fluctuations linked to the formation of first-order lobes (outlined in black with numbers in inset photograph). (c) Detail of part of (b) showing minor pressure fluctuations related to the growth and merger of second-order lobes or finger-like segments (outlined in black in inset photograph).*

4. Discussion

Our experiments reveal the development of complex marginal segments and segment connectors within saucer-shaped intrusions, including pressure variations reflecting the development of these segments. We discuss the implications of these results below by considering how the evolution of the model sills in space and time may contribute to understanding of sill segmentation mechanisms. We also introduce a conceptual model for sill segmentation based on our experimental observations.

4.1. Sill segments and segment connectors

Our experiments have modelled saucer-shaped sills (Figs. 5-6) with complex marginal finger-like and lobe segments, including segment connectors such as bridges and broken bridges. Such features are commonly observed in sedimentary basins such as the Raton, Karoo, Rockall, Faroe-Shetland, Northwest Australian shelf and Neuquén basins (Thomson and Hutton, 2004; Hansen and Cartwright, 2006; Schofield et al., 2012; Magee et al., 2016; Spacapan et al., 2017). The experiments reported here and in Arachchige et al. (Chapter 3), along with previous analogue hydrofracturing experiments using silica flour and clay as analogue host-rock materials (Chang, 2004; Wu, 2006) more closely simulate the natural complexity of sills and their marginal segmentation compared to penny- and saucer-shaped sills formed in sand (Galland et al., 2009; Mathiue et al., 2008) and gelatine (Kavanagh et al., 2006, 2018). This strongly suggests that upper crustal rocks behave as either elasto-plastic or visco-elasto-plastic materials during sill emplacement.

In addition to the rheology of the analogue host-rock material, we have also found that mechanical host-rock layering also controls the nature of sill segment geometries. In our experiments, the marginal segments formed during propagation of the inner sill along the L1/L2 interface are different to those formed when the inclined sheet propagates through the homogenous upper layer. During the inner sill stage, lobes and finger segments define a cyclic

behaviour, showing a sequence of segment formation and coalescence. However, the new lobes and finger-like segments formed after the segment coalescence aren't linked to the previous segments meaning that segment propagation at the interface is history independent. Once the outer sheet forms, the marginal segments become three-dimensional, defining vertically offset, en-echelon, overlapping and/or underlapping segments, which later grow and connect.

Bridges and broken bridges formed by the inflation of segments (Schofield et al., 2012; Magee et al., 2019) also occur in our experiments. These segment connectors only form during the inclined sheet propagation stage of the experiments (Fig. 6). The growth of segment connectors results in the coalescence of segments. Therefore, the inclined sheet intrusion is characterised by a breaking (non-planar) and remerging (almost planar) sequence at the propagating front, which is further supported by the inlet pressure measurement variations (discussed below in 4.3). This suggest that the nature of segments and their connectors evolve sequentially during growth of the experimental intrusions.

4.2. Insights on intrusion segmentation from pressure variations

Pressure variations during experimental sill intrusion (Fig. 8) provide important information for understanding flow dynamics and emplacement mechanisms. Intrusion pressure has been estimated using scaling laws in previous magma emplacement experiments (e.g., Kavanagh et al., 2015). However, fluid pressure is often directly measured in hydro-fracturing experiments (Chang, 2004; Wu, 2006; Hurt, 2012). Laboratory hydro-fractures described in Murdoch (1993a) and Chang (2004) using Center Hill clay and Georgia Red clay as analogue host rocks, respectively, show similar complex marginal segmentation structures to our model intrusions. Furthermore, the pressure curves of hydro-fractures measured by Chang (2004) and Wu (2006) reflect the formation of lobes during fracture segmentation. In Chang (2004), the injection pressure for fractures formed within Georgia Red Clay reached a peak value of ~1400 MPa and pressure drops up to 350 MPa during final stage of the crack.

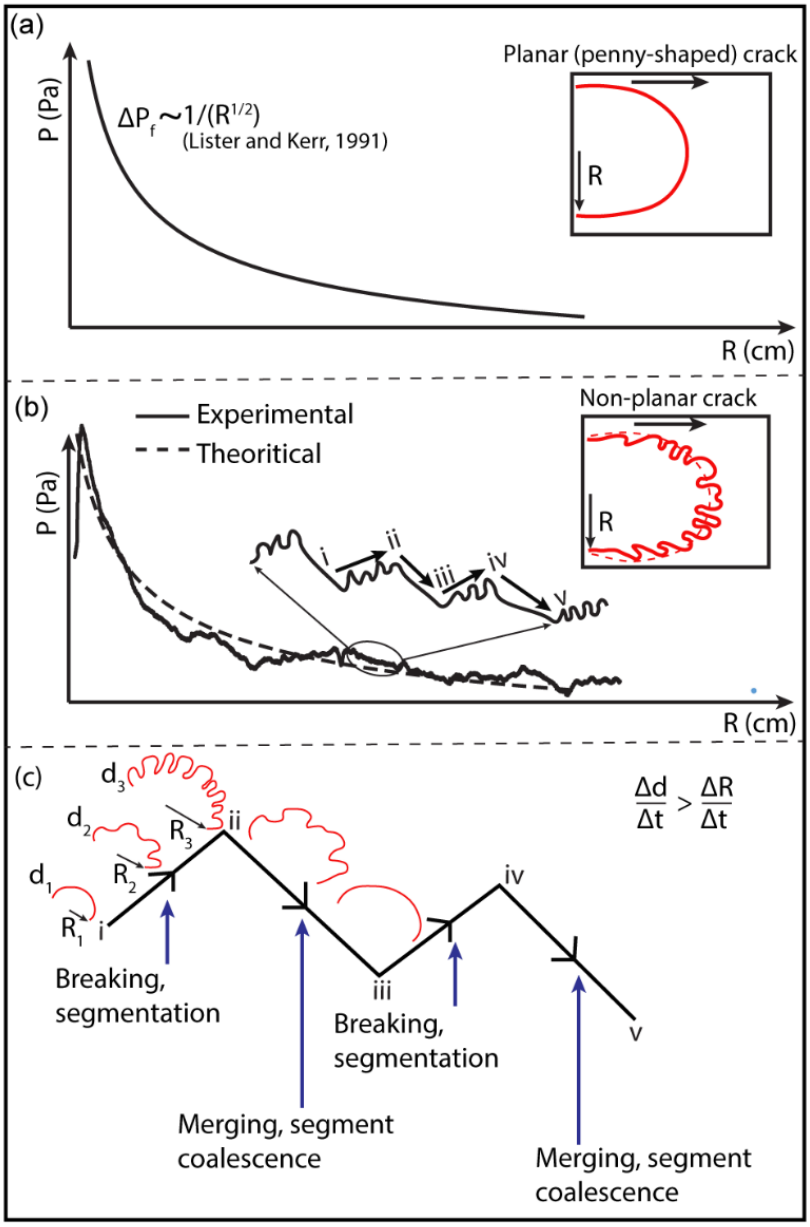

Figure 9: *Schematic pressure curves for (a) an ideal penny-shaped crack (Chang, 2004; Lister and Kerr, 1991) and (b) a non-planar experimental curve (Exp 5) superimposed on an ideal penny-shaped crack (dotted lines). (c) Interpretation of smaller scale pressure fluctuations highlighted in (b). During the initial growth of segments, the planar margin breaks down (i→ii; Fig. 8c) and the pressure rises due to a faster increase of the outer perimeter* $(\frac{\Delta d}{\Delta t})$ *compared to rate of change of sill radius* $(\frac{\Delta R}{\Delta t})$*. Conversely, during subsequent stages of remerging/coalescence of segments (ii → iii), the pressure decreases as the rate of growth of the outer perimeter decreases. Note that, during transient pressure peaks or troughs, the change in intrusion radius (e.g.* $R_3–R_1$*) is smaller compared to the change in intrusion parameter* $(d_3–d_1)$*. R – intrusion radius, d – intrusion perimeter, t – time.*

463 The maximum pressure measured during hydrofracture formation in Wu (2006) was
464 between 6500 – 8000 MPa, decreasing to 500 – 3750 MPa, respectively. These measurements
465 are three-orders of magnitude higher than the peak (2.8×10^{-3} MPa) and range of pressures (1.9
466 – 2.8×10^{-3} MPa) observed during the crack growth in our LRD experiments, although they
467 show similar pressure fluctuations associated with the formation of segments. However, the
468 differences in pressures in Chang (2004) and Wu (2006) to our results are mainly due to the
469 use of virtually cohesionless dry particulate materials and the applied axial loads, respectively.
470 The fluid pressure (ΔP_f) required to propagate an ideal, fluid-filled penny-shaped crack is
471 predicted to gradually decrease with increasing crack radius (R), according to the theoretical
472 relationship (Lister and Kerr, 1991)

473 $$\Delta P_f \sim 1/ (R^{1/2}) \quad (4)$$

474 The pressure curve in Figure 9a was generated to compare this theoretical prediction
475 with experimental data, and it can move along the y-axis depending on the fracture toughness
476 (K_c) of the material ($\Delta P_f \sim K_c/R^{1/2}$), which is not well constrained for the LRD gels used in our
477 experiments (Lister and Kerr, 1991; Chang, 2004). The pressure drop observed in Exp. 5
478 follows the general behaviour predicted by Eq. 4, with minor superimposed fluctuations as
479 described above (Figs. 8a-b, 9b).

480 We interpret short periods of increasing pressure during sill growth (Figs. 9b and 9c;
481 i→ii) to record segmentation events at the propagating sill margin. In Fig. 9b, we fit the Exp.
482 5 pressure curve to the theoretical curve by assuming the fracture toughness of the LRD is
483 similar to that of in theoretical curve. The perimeter (d) of an ideal penny-shaped crack
484 increases with the radius according to $d = 2\pi R$. As the degree of marginal segmentation
485 increases, the total outer perimeter of the propagating sill increases at a rate that is greater that
486 of an ideal penny-shaped crack, resulting in a transient increase in pressure. The opposite
487 happens during periods of transient pressure decrease (Figs. 9b and 9c; ii → iii), which we

attribute to segment coalescence and an overall decrease in the perimeter length to a value that approaches that of an ideal penny shaped crack We therefore interpret the observed transient pressure fluctuations (Figs. 8b-c) to reflect periods of marginal segmentation and segment coalescence, which in turn drive changes in the rate of perimeter growth versus sill radius growth.

4.3. Conceptual model for sill segmentation

Two brittle fracturing mechanisms can lead to the formation of segments during emplacement of sills into brittle-elastic host rocks: (i) rotation of the principal stress axes ahead of the propagating fracture (Pollard et al., 1982; Nicholson and Pollard, 1985; Takada, 1990; Schofield et al., 2012); and (ii) exploitation of preferentially oriented, pre-existing weaknesses (Hutton, 2009; Schofield et al., 2012; Stephens et al., 2017). In the first mechanism, a change of stress orientation at the propagating front is likely due to the onset of mixed-mode loading (Mode I+II, Mode I+III), which results in twisting and splitting of the sill tip into en-echelon segments with a consistent stepping direction (Pollard et al., 1982; Nicholson and Pollard, 1985). In the second mechanism, sills emplaced into layered sedimentary strata can become segmented with inconsistent stepping direction as they follow pathways of least resistance (e.g., bedding planes, fault planes).

However, inelastic mechanisms, such as ductile flow, shear faulting and granular flow (e.g., fluidisation) can also result in segment formation (Pollard et al., 1975; Thomson and Hutton, 2004; Schofield et al., 2012; Magee et al., 2016; Spacapan et al., 2017). Viscous-fingering instabilities (e.g., Saffman-Taylor instability) between a propagating magma front and a fluid host rock have previously been invoked as a mechanism of magma finger initiation (Pollard et al., 1975; Schofield et al., 2010). Moreover, a recent analysis by Ball et al. (2021, and references therein) show that visco-plastic Saffmann-Talyor instabilities can also form

fracture fronts that are similar to magma fingers in both nature (Schofield et al., 2010) and the laboratory experiments reported here (Arachchige et al., 2021; Chapter 3 and 4).

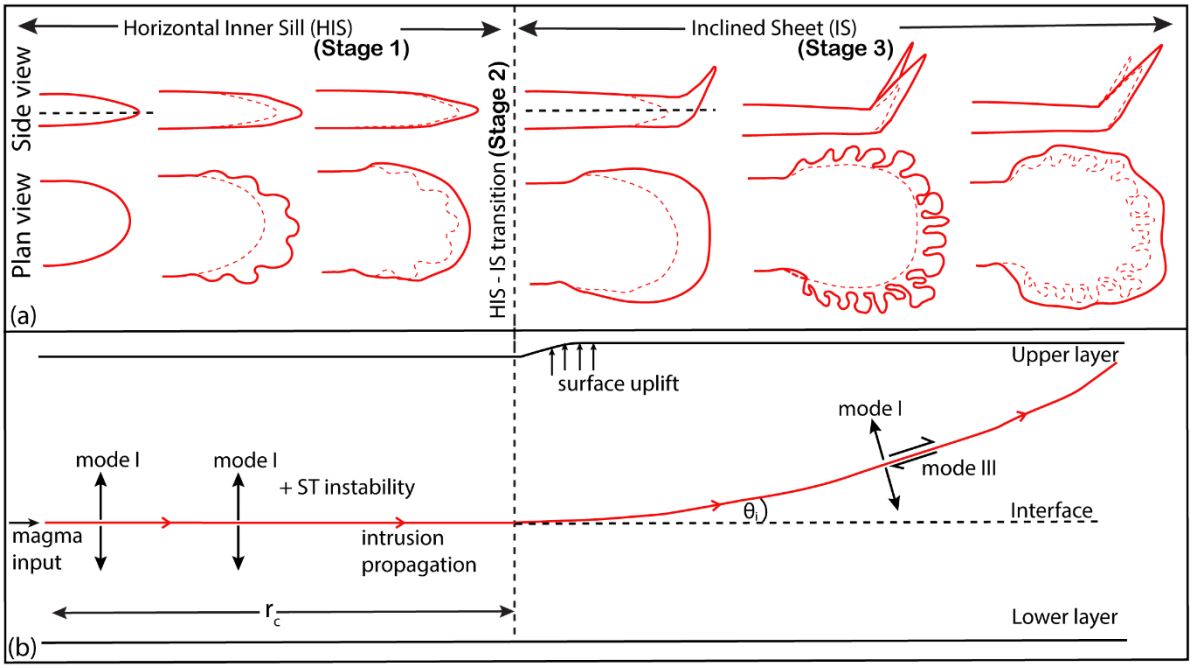

Figure 10: *Conceptual model for segment evolution within a saucer-shaped sill. (a) Side and plan views of propagating sill front geometries during: (i) the horizontal inner sill (Stage 1), (ii) the inner sill to inclined sheet transition (Stage 2), and iii) the inclined outer sheet (Stage 3). The continuous and dashed red lines represent active and previous propagating margins, respectively. (b) Simplified cross-sectional (schematic) view of the intrusion shown in (a) and the related emplacement mechanisms. Mode I – elastic fracture opening (planar). Mixed-mode (I+III) – breaking/twisting of the propagating front (segmentation).*

Using this framework, and the sill segment and segment connector geometries and pressure curves recorded in our experiments, we propose the following multi-stage model for sill propagation and segmentation:

Stage 1: Emplacement and propagation of the horizontal inner sill (HIS) along a pre-existing horizontal interface (Fig. 10). A penny-shaped sill with a planar margin is initially emplaced as a Mode I fracture (opening mode) controlled by magma overpressure and the elastic response of the host rock, consistent with predictions from linear elastic fracture mechanics (LEFM) (e.g., Pollard and Holzhausen, 1979). The lobe and finger-like segments then start to emerge from the planar front without any offset or stepping, which suggests that

527 the brittle-elastic LEFM mechanisms may not apply. Therefore, the marginal lobes and finger-
528 like segments observed in this stage (Fig. 10b, Stage 1) are more likely linked to small-scale
529 (< 1cm) visco-plastic version of Saffman-Taylor instabilities (Ball et al., 2021) occurring at the
530 tip of the propagating sills. Segments will then propagate and grow provided there is sufficient
531 driving pressure, and once they reach a critical dimension, segment coalescence then occurs to
532 reform a planar sill front. This cyclic behaviour continues until the sill starts to propagate within
533 the upper homogenous layer.

534 *Stage 2:* Transition from a horizontal inner sill (HIS) to an inclined outer sheet (IS) (Fig.
535 10; Stage 2). When the HIS reaches a critical radius (r_c) of approximately the thickness of the
536 overburden (H) (i.e. $0.5 \leq r_c/H \leq 2.5$; Arachchige et al. Chapter 3), the sill becomes inclined
537 relative to the L1/L2 interface and the free surface, forcing the stress at the sill tip to become
538 asymmetric. Due to the elastic dominant interaction between the propagating sill and the upper
539 free surface (Pollard and Holzhausen, 1979; Galland et al., 2008) the sill also climbs upwards
540 due to the asymmetry of the stress field caused by the uplift of the overburden.

541 *Stage 3:* Sill segmentation within the inclined sheet (Fig. 10; Stage 3). Within the outer
542 inclined sheet, sill propagation is no longer controlled by the anisotropy of the L1/L2 interface
543 and the intrusion evolves in 3D. Propagation of the inclined sheet may cause surface uplift or
544 force folding in the overburden, which will change the principal stress orientations (Fig. 10b).
545 These changes at the sill front lead to 3D segmentation (> 1cm), which can be attributed to the
546 mixed mode (Mode I+III) loading. In this case, the mode III component might be related to: (i)
547 the 3D fracture geometry; (ii) flow front instability; or (iii) interactions with the side and upper
548 boundaries. Unlike Stage 1, the segments are either co-planar and/or multi planar, with
549 horizontal and vertical offsets. Inflation of these segments results in the formation of segment
550 connectors such as bridges and broken bridges (Schofield et al., 2012; Magee et al., 2019). The

margin then becomes planar (or quasi-planar) due to the connection of segments through bridges and broken bridges.

Our conceptual model provides an evolutionary framework for sill segmentation within saucer-shaped intrusions. The marginal lobes and finger-like segments observed within the interface (i.e., inner sill) and the homogenous upper layer (i.e., inclined sheet) in our experiments are more likely linked to small-scale (< 1cm) visco-plastic deformation instabilities occurring at the tip of the propagating sills and large-scale (>1 cm) mixed mode (Mode I+III) loading, respectively . This suggests the operation of scale-dependent deformation processes, with brittle-elastic (LEFM) processes dominating at the whole of intrusion scale and visco-plastic processes dominating at the crack tip scale. Moreover, the model is consistent with field and 3D seismic observations of sills and dykes in the shallow brittle upper crust. Importantly, it provides insights on the evolution of segments and segment connectors in time and space as an intrusion propagates in 3D.

5. Conclusions

We present a detailed geometrical analysis of sill segmentation in a series of saucer-shaped sill emplacement experiments. Paraffin oil (model magma) is injected at constant flow rate into a layered, visco-elasto-plastic Laponite RD® (model crust). Our key conclusions are:

1. Th emodelled saucer-shaped sills have complex geometries and highly segmented margins consisting of fingers and lobes in both the inner flat sill, following a horizontal layer interface, and the outer inclined sheet where the segments exploit a 3D volume around the sill tip.

2. Due to the influence of the interface, the flat section of the intrusion is limited to co-planar segments and therefore no segment connectors formed. However, out of plane segments form within the inclined sheet that lead to the formation of segment connectors due to segment overlap and inflation.

3. Based on quantitative measurements of segment geometries, we determined that the segments have bimodal behaviour: i) interface-controlled aspect ratios (mode 1) forming wide lobes; and ii) homogenous layer-controlled aspect ratios (mode 2) forming narrow and long segments.

4. The pressure signatures measured during saucer-shape sill intrusion can be linked to periods of marginal segmentation and coalescence. Transient increases during sill propagation occur during period of increased segmentation, as the rate of perimeter growth increases, whereas transient pressure drops occur during segment coalescence, as the rate of perimeter growth decreases.

5. Our experiments suggest that segments and segment connectors evolve in space and time through multi-stage emplacement mechanisms. We present a conceptual sill segmentation model to account for the variety and sequence of segment geometries. We propose that the small-scale segments within the interface and the large-scale segments on inclined sheets are due to the visco-plastic instabilities and brittle-elastic fracturing, respectively.

Acknowledgements

We gratefully acknowledge support from an Australian Research Council Discovery Grant (DP190102422) to A.R.C., Dean's International Postgraduate Research Scholarship (DIPRS) and Graduate Research Completion Award (GRCA) scholarship from Monash University (Melbourne) to U.S.N.A.

References

Anderson, E.M., 1937. The Dynamics of the Formation of Cone-sheets, Ring-dykes, and Caldron-subsidences. Proceedings of the Royal Society of Edinburgh 56, 128–157. https://doi.org/10.1017/s0370164600014954

Arachchige, U.N., Cruden, A.R., Weinberg, R., 2021. Laponite gels - visco-elasto-plastic analogues for geological laboratory modelling. Tectonophysics 805, 228773.

https://doi.org/10.1016/j.tecto.2021.228773

Ball, T. V., Balmforth, N.J., Dufresne, A.P., 2021. Viscoplastic fingers and fractures in a Hele-Shaw cell. Journal of Non-Newtonian Fluid Mechanics 289, 104492. https://doi.org/10.1016/j.jnnfm.2021.104492

Bertelsen, H.S., Rogers, B.D., Galland, O., Dumazer, G., Abbana Benanni, A., 2018. Laboratory Modeling of Coeval Brittle and Ductile Deformation During Magma Emplacement Into Viscoelastic Rocks. Frontiers in Earth Science 6. https://doi.org/10.3389/feart.2018.00199

Bunger, A.P., Jeffrey, R.G., Detournay, E., 2008. Evolution and morphology of saucer-shaped sills in analogue experiments. Geological Society Special Publication 302, 109–120. https://doi.org/10.1144/SP302.8

Chanceaux, L., Menand, T., 2016. The effects of solidification on sill propagation dynamics and morphology. Earth and Planetary Science Letters 442, 39–50. https://doi.org/10.1016/j.epsl.2016.02.044

Chang, H., 2004. Hydraulic fracturing in particulate materials, Ph.D. thesis. Georgia Institute of Technology, GA. 267.

Cruden, A.R., Weinberg, R.F., 2018. Mechanisms of magma transport and storage in the lower and middle crust-magma segregation, ascent and emplacement. Volcanic and Igneous Plumbing Systems: Understanding Magma Transport, Storage, and Evolution in the Earth's Crust. 13–53. https://doi.org/10.1016/B978-0-12-809749-6.00002-9

Currier, R.M., Marsh, B.D., 2015. Mapping real time growth of experimental laccoliths: The effect of solidification on the mechanics of magmatic intrusion. Journal of Volcanology and Geothermal Research 302, 211–224. https://doi.org/10.1016/j.jvolgeores.2015.07.009

Delaney, P., Pollard, D., 1981. Deformation of Host Rocks and Flow of Magma during Growth

of Minette Dikes and Breccia-bearing Intrusions near Ship Rock , New Mexico. Geological Survey Professional Paper 69.

Eide, C.H., Schofield, N., Jerram, D.A., Howell, J.A., 2017. Basin-scale architecture of deeply emplaced sill complexes: Jameson Land, East Greenland Christian. Journal of the Geological Society 174, 23–40. https://doi.org/10.1144/jgs2016-018

Ernst, R.E., Head, J.W., Parfitt, E., Grosfils, E., Wilson, L., 1995. Giant radiating dyke swarms on Earth and Venus. Earth Science Reviews 39, 1–58. https://doi.org/10.1016/0012-8252(95)00017-5

Galland, O., Planke, S., Neumann, E.R., Malthe-Sørenssen, A., 2009. Experimental modelling of shallow magma emplacement: Application to saucer-shaped intrusions. Earth and Planetary Science Letters 277, 373–383. https://doi.org/10.1016/j.epsl.2008.11.003

Galland, O., Spacapan, J.B., Rabbel, O., Mair, K., Soto, F.G., Eiken, T., Schiuma, M., Leanza, H.A., 2019. Structure, emplacement mechanism and magma-flow significance of igneous fingers – Implications for sill emplacement in sedimentary basins. Journal of Structural Geology 124, 120–135. https://doi.org/10.1016/j.jsg.2019.04.013

Griffiths, R.W., 2000. The Dynamics of Lava Flows. Annual Review of Fluid Mechanics 32, 477–518. https://doi.org/10.1146/annurev.fluid.32.1.477

Hansen, D.M., Cartwright, J., 2006. Saucer-shaped sill with lobate morphology revealed by 3D seismic data: implications for resolving a shallow-level sill emplacement mechanism. Journal of the Geological Society 163, 509–523. https://doi.org/10.1144/0016-764905-073

Hubbert, M.K., 1937. Theory of scale models as applied to the study of geologic structures. GSA Bulletin 48, 1459–1520. https://doi.org/10.1130/GSAB-48-1459

Hurt, R.S., 2012. Toughness-Dominated Hydraulic Fractures in Cohesionless Particulate Materials, Ph.D. thesis. Georgia Institute of Technology, GA.

650 Hutton, D.H.W., 2009. Insights into magmatism in volcanic margins: bridge structures and a
651 new mechanism of basic sill emplacement - Theron Mountains, Antarctica. Petroleum
652 Geoscience 15, 269–278. https://doi.org/10.1144/1354-079309-841
653 Kavanagh, J.L., Boutelier, D., Cruden, A.R., 2015. The mechanics of sill inception,
654 propagation and growth: Experimental evidence for rapid reduction in magmatic
655 overpressure. Earth and Planetary Science Letters 421, 117–128.
656 https://doi.org/10.1016/j.epsl.2015.03.038
657 Kavanagh, J.L., Menand, T., Daniels, K.A., 2013. Gelatine as a crustal analogue: Determining
658 elastic properties for modelling magmatic intrusions. Tectonophysics 582, 101–111.
659 https://doi.org/10.1016/j.tecto.2012.09.032
660 Kavanagh, J.L., Menand, T., Sparks, R.S.J., 2006. An experimental investigation of sill
661 formation and propagation in layered elastic media. Earth and Planetary Science Letters
662 245, 799–813. https://doi.org/10.1016/j.epsl.2006.03.025
663 Lister, J.R., Kerr, R.C., 1991. Fluid-mechanical models of crack propagation and their
664 application to magma transport in dykes. Journal of Geophysical Research 96, 10049.
665 https://doi.org/10.1029/91JB00600
666 Magee, C., Muirhead, J., Schofield, N., Walker, R.J., Galland, O., Holford, S., Spacapan, J.,
667 Jackson, C.A., Mccarthy, W., 2018. Structural signatures of igneous sheet intrusion
668 propagation Craig. Journal of Structural Geology.
669 https://doi.org/10.1016/j.jsg.2018.07.010.This
670 Magee, C., Muirhead, J., Schofield, N., Walker, R.J., Galland, O., Holford, S., Spacapan, J.,
671 Jackson, C.A.L., McCarthy, W., 2019. Structural signatures of igneous sheet intrusion
672 propagation. Journal of Structural Geology 125, 148–154.
673 https://doi.org/10.1016/j.jsg.2018.07.010
674 Magee, C., Muirhead, J.D., Karvelas, A., Holford, S.P., Jackson, C.A.L., Bastow, I.D.,

675 Schofield, N., Stevenson, C.T.E., McLean, C., McCarthy, W., Shtukert, O., 2016. Lateral
676 magma flow in mafic sill complexes. Geosphere 12, 809–841.
677 https://doi.org/10.1130/GES01256.1
678 Mathieu, L., van Wyk de Vries, B., Holohan, E.P., Troll, V.R., 2008. Dykes, cups, saucers and
679 sills: Analogue experiments on magma intrusion into brittle rocks. Earth and Planetary
680 Science Letters 271, 1–13. https://doi.org/10.1016/j.epsl.2008.02.020
681 Miles, A., Cartwright, J., 2010. Hybrid flow sills: A new mode of igneous sheet intrusion.
682 Geology 38, 343–346. https://doi.org/10.1130/G30414.1
683 Muirhead, J.D., Van Eaton, A.R., Re, G., White, J.D.L., Ort, M.H., 2016. Monogenetic
684 volcanoes fed by interconnected dikes and sills in the Hopi Buttes volcanic field, Navajo
685 Nation, USA. Bulletin of Volcanology 78, 1–16. https://doi.org/10.1007/s00445-016-
686 1005-8
687 Murdoch, L.C., 1993a. Hydraulic fracturing of soil during laboratory experiments Part 2.
688 Propagation. Geotechnique 43, 255–265. https://doi.org/10.1680/geot.1993.43.2.255
689 Murdoch, L.C., 1993b. Hydraulic fracturing of soil during laboratory experiments Part 1 .
690 Methods and observations. Geotechnique 43, 255–265.
691 https://doi.org/10.1680/geot.1993.43.2.255
692 Nicholson, R., Pollard, D.D., 1985. Dilation and linkage of echelon cracks. Journal of
693 Structural Geology 7, 583–590. https://doi.org/10.1016/0191-8141(85)90030-6
694 Norris, J., Giese, R.F., Costanzo, P.M., Vanoss, C.J., 1993. The Surface Energies of Cation
695 Substituted Laponite. Clay Minerals 28, 1–11.
696 https://doi.org/10.1180/claymin.1993.028.1.01
697 Pollard, D., Delaney, P.T., Segall, P., 1982. Formation and interpretation of dilatant echelon
698 cracks. Geological Society of America Bulletin 93, 1291–1303.
699 https://doi.org/10.1130/0016-7606(1982)93<1291:faiode>2.0.co

Pollard, D., Johnson, M., 1973. David d. pollard. Tectonophysics 18, 311–354.

Pollard, D.D., 1973. Derivation and evaluation of a mechanical model for sheet intrusions. Tectonophysics 19, 233–269. https://doi.org/10.1016/0040-1951(73)90021-8

Pollard, D.D., Holzhausen, G., 1979. On the mechanical interaction between a fluid-filled fracture and the earth's surface. Tectonophysics 53, 27–57. https://doi.org/10.1016/0040-1951(79)90353-6

Pollard, D.D., Muller, O.H., Dockstader, D.R., 1975. The form and growth of fingered sheet intrusions. Bulletin of the Geological Society of America 86, 351–363. https://doi.org/10.1130/0016-7606(1975)86<351:TFAGOF>2.0.CO;2

Ramberg, H., 1967. Model Experimentation of the Effect of Gravity on Tectonic Processes. Geophysical Journal of the Royal Astronomical Society 14, 307–329. https://doi.org/10.1111/j.1365-246X.1967.tb06247.x

Rubin, A.M., 1993. Tensile fracture of rock at high confining pressure Implications for dike propagation. Journal of Geophysical Research 98, 919–935.

Ruzicka, B., Zaccarelli, E., 2011. A fresh look at the Laponite phase diagram. Soft Matter 7, 1268–1286. https://doi.org/10.1039/c0sm00590h

Schofield, N., Heaton, L., Holford, S.P., Archer, S.G., Jackson, C.A.L., Jolley, D.W., 2012. Seismic imaging of "broken bridges": Linking seismic to outcrop-scale investigations of intrusive magma lobes. Journal of the Geological Society 169, 421–426. https://doi.org/10.1144/0016-76492011-150

Schofield, N., Stevenson, C., Reston, T., 2010. Magma fingers and host rock fluidization in the emplacement of sills. Geology 38, 63–66. https://doi.org/10.1130/G30142.1

Schofield, Brown, D.J., Magee, C., Stevenson, C.T., 2012. Sill morphology and comparison of brittle and non-brittle emplacement mechanisms. Journal of the Geological Society 169, 127–141. https://doi.org/10.1144/0016-76492011-078

Spacapan, J.B., Galland, O., Leanza, H.A., Planke, S., 2017. Igneous sill and finger emplacement mechanism in shale-dominated formation: a field study at Cuesta del Chihuido, Neuquén Basin, Argentina. Journal of the Geological Society 174, 422–433. https://doi.org/10.1144/jgs2016-056

Spence, D.A., Turcotte, D.L., 1985. Magma-driven propagation of cracks. Journal of Geophysical Research 90, 575–580.

Stephens, T.L., Walker, R.J., Healy, D., Bubeck, A., England, R.W., McCaffrey, K.J.W., 2017. Igneous sills record far-field and near-field stress interactions during volcano construction: Isle of Mull, Scotland. Earth and Planetary Science Letters 478, 159–174. https://doi.org/10.1016/j.epsl.2017.09.003

Takada, A., 1990. Experimental Study on Propagation of Liquid-Filled Crack in Gelatin : Shape and Velocity in Hydrostatic Stress Condition. 95, 8471–8481.

Thomson, K., Hutton, D., 2004. Geometry and growth of sill complexes: Insights using 3D seismic from the North Rockall Trough. Bulletin of Volcanology 66, 364–375. https://doi.org/10.1007/s00445-003-0320-z

Wu, R., 2006. Some Fundamental Mechanisms of Hydraulic Fracturing, Ph.D. thesis. Georgia Institute of Technology, GA. 301.